PREDIS

Extension to:
D7.5. Report on the Digital Twin of a cemented waste package, geochemical evolution and mechanical integrity modelling

Characterization experiments at KIT-INE of an old LLW drum (in cooperation with PSI-LES)

31.07.2024 Version Final

Dissemination level: Public

P. G. Szabo[1], X. Gaona[1], D. Rehhorn[1], O. Dieste Blanco[1], D. Schild[1], T. Prüßmann[1], N. Müller[1], R. E. Guidone[1], R. Dähn[2], M. Altmaier[1]

[1]Karlsruhe Institute of Technology, Institute for Nuclear Waste Disposal, Karlsruhe (Germany)
[2]Paul Scherrer Institute, Nuclear Energy and Safety Department, Laboratory for Waste Management, Villigen (Switzerland)

xavier.gaona@kit.edu
+49 721 608 26134

Project acronym PREDIS	Project title PRE-DISposal management of radioactive waste		Grant agreement No. 945098	
Deliverable No. 7.5 (Extension)	Deliverable title Characterization experiments at KIT-INE of an old LLW drum (in cooperation with PSI-LES)			Version Final
Type Report	Dissemination level Public			Due date M42
Lead beneficiary KIT				WP No. 7
Main author Xavier Gaona (KIT)	Reviewed by Christian Köpp (BAM)		Accepted by Maria Oksa (VTT), Coordinator	
Contributing author(s) P. G. Szabo (KIT), X. Gaona (KIT), D. Rehhorn (KIT), O. Dieste Blanco (KIT), D. Schild (KIT), T. Prüßmann (KIT), N. Müller (KIT), R. E. Guidone (KIT), R. Dähn (PSI), M. Altmaier (KIT)				Pages 23

Abstract

This report summarizes the work performed at KIT-INE on the characterization of a LLW cemented waste drum stored since 1994 at the Swiss Federal Interim Storage Facility (BZL), which is operated by PSI. After approval of the Swiss Federal Nuclear Safety Inspectorate (ENSI) these drums were opened. Cement samples from four different locations in the drum (bottom, middle, upper, lid top part) were collected by PSI and sent to KIT-INE. A multi-method approach was used for the characterization of these samples, including X-ray diffraction (XRD), thermogravimetric analysis coupled to differential scanning calorimetry (TGA-DSC), X-ray photoelectron spectroscopy (XPS), scanning electron microscopy and energy dispersive X-ray spectroscopy (SEM-EDS), as well as micro computed tomography (μ-CT). To account for heterogeneities in the sample, different aliquots of each drum location were investigated.

Characterization methods consistently confirmed the presence of quartz, C-S-H, portlandite, calcite and ettringite phases. The predominance of quartz is consistent with the large fraction of this phase in the original formulation. Heterogeneities of the material are supported by all characterization techniques. No clear trends are observed along the investigated drum, with the exception of a systematic decrease in the overall Ca:Si ratio from the top to the bottom of the cemented drum. Insights on the porosity of the material are obtained by μ-CT, with the identification of two main regions of manifestly different porosity.

Keywords

LLW, cemented waste drum, multi-method approach, XRD, TGA-DSC, XPS, SEM-EDS, μ-CT

Table of Contents

1 Material investigated

The LLW drum investigated in this work was stored since 1994 at the Swiss Federal Interim Storage Facility (BZL) in Villigen, operated by PSI. The selected drum was sectioned in four main fragments, defined along this report as lid top, upper, middle and bottom fragments (see Figure 1). For sampling, the steel shell of the barrels was first removed using a grinder. The cement blocks were then cut out using a diamond cutting blade.
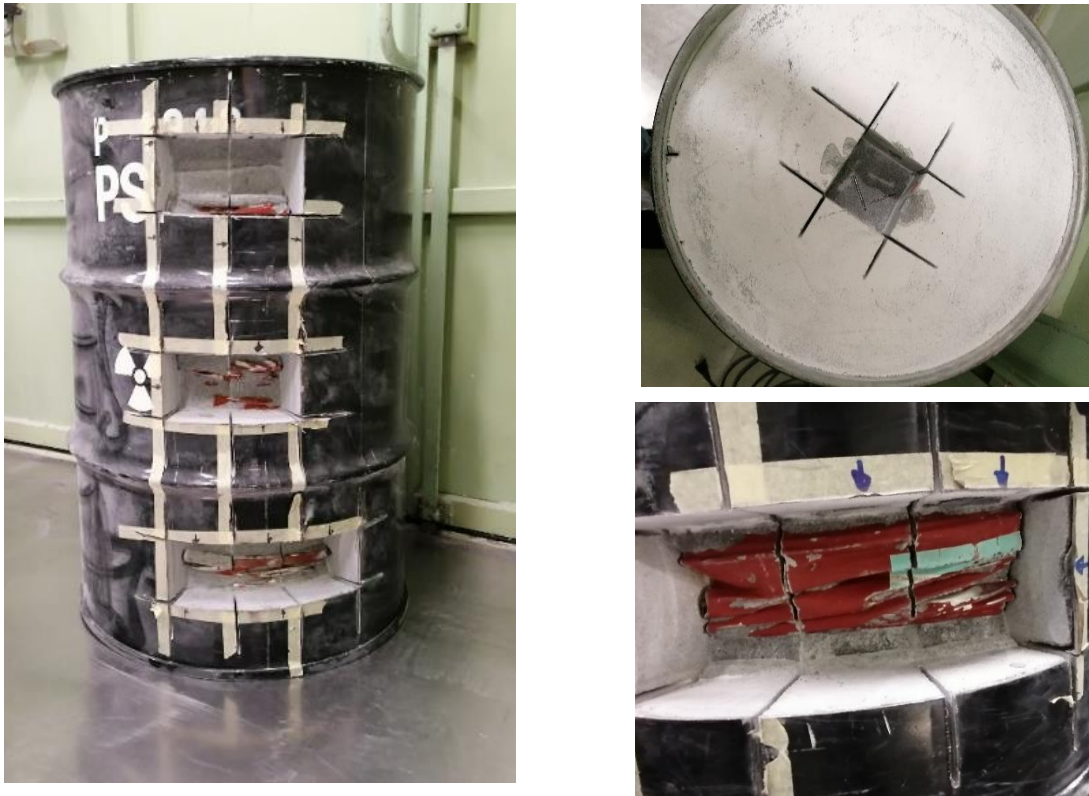

Figure 1. *Cemented old LLW drum considered for the multi-method characterization within this study. Samples were taken at PSI from lid top, upper, middle and bottom fragments.*

The cement blocks received at KIT-INE were first crushed and grinded to fragments of approximately < 1 cm under ambient conditions. A fraction of these fragments was further crushed in mortar in order to get fine particle sized of approximately < 100 μm. The larger fragments resulting from the first grinding step were characterized by micro computed tomography (μ-CT) and scanning electron microscopy – energy dispersive X-ray spectroscopy (SEM-EDS), whereas the finer cement powders generated in the second crushing step were characterized by X-ray diffraction (XRD), X-ray photoelectron spectroscopy (XPS) and thermogravimetric analysis coupled with differential scanning calorimetry (TGA–DSC).

The composition of the cementitious material used in the solidification of the LLW drum is summarized in Table 1.

Table 1. Chemical composition of the cement material used in the solidification of the LLW drum investigated in this work (Dähn, personal communication). Values provided in parts per weight. Sperrbarra Plus OL stands for the commercial name of the superplasticizer used in the formulation.

Components	HTS-cement	Micropoz	Clinoptilolith	Quartz sand	Sperrbarra Plus OL	water	w/c
Fraction	100	30	15	156	2.0	59	0.6

2 Characterization methods

2.1 XRD

The fine cement particles of cement blocks were mixed with ethanol, and the resulting suspensions placed on a crystal silicon plate, which was dried at room temperature under air. A D8 Advance (Bruker AXS) diffractometer with an energy-dispersive detector (Cu Kα radiation) was used to collect the diffraction patterns of different cement samples. Diffractograms were collected within $5° \leq 2\Theta \leq 90°$, with step size of 0.011° and a counting time of 0.5 second per step. Raw data were evaluated using the Bruker AXS Diffracplus EVA software, and collected patterns compared with reference data in the JCPDS database [1]. The average crystallite size of the different phases was determined using the Scherrer-equation [5, 11]. The Scherrer equation is generally considered accurate for crystallite size of up to 100–200 nm [5]. The Diffracplus EVA software used in this work allows the determination of crystallite sizes of up to 500 nm, which has been considered as upper limit in this work. Peak fitting was achieved using asymmetrical Split Pseudo Voigt function [10].

2.2 XPS

XPS measurements were performed using a PHI 5000 Versa Probe II (ULVAC-PHI Inc.) spectrometer equipped with a scanning microprobe X-ray source (monochromatic Al Kα (1486.7 eV) X-rays) in combination with an electron flood gun and a floating ion gun generating low energy electrons (1.0 eV) and low energy argon ions (8 eV) for charge compensation at isolating samples (dual beam technique), respectively. The samples were prepared by grinding the investigated cement powder, which was afterwards pressed onto an indium foil. Survey scans were recorded with an X-ray source power of 31 W and pass energy of 187.85 eV. Narrow scans of the elemental lines were recorded at 23.5 eV pass energy, which yields an energy resolution of 0.69 eV FWHM at the Ag $3d_{5/2}$ elemental line of pure silver. Calibration of the binding energy scale of the spectrometer was performed using well-established binding energies of elemental lines of pure metals (monochromatic Al Kα: Cu $2p_{3/2}$ at 932.62 eV, Au $4f_{7/2}$ at 83.96 eV) [12]. Error of binding energies of insulating samples is estimated within ± 0.2 eV. The C 1s elemental line of adventitious hydrocarbon at 284.8 eV was used for charge referencing, which corresponds to a binding energy of Si 2p at 103.0 eV. Atomic concentrations are calculated from the areas of elemental lines (after Shirley background subtraction) of survey spectra using sensitivity factors of the elemental lines, asymmetry parameters, and transmission function of the analyzer. Narrow scans of elemental lines were recorded for determination of chemical shifts and spectral features. Binding energies of elemental lines are compared to reference data [8, 9]. Data analysis was performed using ULVAC-PHI MultiPak Version 9.7.

2.3 TGA-DSC

TGA-DSC/DTG characterization was carried out with a STA409 (Netzsch Gerätebau GmbH) apparatus under inert gas atmosphere (N_2). Fractions of approximately 50 mg per sample were placed in a Al_2O_3 crucible and sample holder of type S Pt 10% /Pt-Rh. Samples were heated from ~25°C to 1200°C with a heating rate of 10 °C/min.

2.4 μ-CT and SEM-EDS

The original cement blocks sealed in plastic bags were analysed by μ-CT using a Zeiss 620 Versa instrument. The X-ray source was set to 160 kV accelerating voltage with a power of 25 W. 1601 projection images were recorded with 0.3 s integration time each using a flatpanel detector. The voxel size after reconstruction was $(44.76)^3$ μm³. Electron microscope (EM) images and Energy Dispersive X-ray Spectrometry (EDS) analysis was performing using focused ion beam scanning electron microscopy (FIB-SEM) - Zeiss FIB-SEM, model Crossbeam 350 KMAT (hereafter Crossbeam 350), with integrated laser ablation module. This model consists of: field emission gun and GEMINI 2 electron optical column for high resolution analysis. The GEMINI 2 objective lens generates a fine focused electron beam, with resolution of 0.9 nm at 15 kV and 1.7 nm at 1 kV without beam deceleration. Accelerating voltage ranges from 0.02-30 kV, beam current from 1 pA - 100 nA. Scanning Electron Microscope (SEM) is equipped with different detectors, e.g. secondary electrons (Everhart-Thornley SE detector for morphology) and backscattered electrons (BSE) (compositional/material contrast) detectors. Additionally, Crossbeam 350 is equipped with InLens secondary and backscattered electron detection, best applicable at accelerating voltages below 5 kV. Images are recorded in 4:3 format with 16-bit dynamic range and various resolution; here the resolution was set to 3072 x 2304 pixels. Workstation allows to perform Energy Dispersive X-ray Spectrometry (EDS) analysis utilizing UltimMAX100 (100 mm^2) silicon drift detector to determine elemental distribution and run a composition analysis of materials in SEM (SEM-EDS). The electronics have very low noise, allowing for accurate identification and characterization of X-ray lines down to 72 eV. Results were displayed as elemental maps, where EDS spectrum can be reconstructed on the feature/area of interest. Mapping was done using 1024 and 2048 channels and resolution of 2048 x 1536 pixels with dwell time set to 50 μs and 120 μs, respectively. Acceleration voltage spanned from 5 kV to 20 kV. The EDS data recording and data processing is done using AZtec 6.0 SP2 software by Oxfords Instruments.

3   Results and discussion

3.1   XRD and crystallite size of phase constituents

XRD patterns of the cement fragments collected from the waste drum are presented in Figures 2-3. Two independent sub-samples were characterized from each drum region. Figure 2 shows an overview of the XRD patterns collected for the four evaluated regions in the waste drum (bottom, middle, up, top lid; see Figure 1). Although many patterns are consistent throughout all drum regions, diffractograms in Figure 2 reflect the heterogeneous character of the investigated material. The strongest reflections in Figure 2 and Figure 3a observed at $2\Theta \approx 20.9$ and 26.6 degree are assigned to quartz (PDF 85-0795), corresponding to unreacted quartz sand originally present in the cement formulation. In the same figure, feature at $2\Theta \approx 29.5$ degree supports the presence of calcite in almost all fragments evaluated. The presence of calcite is also confirmed by TGA-DTA (see Section 3.3), and underpins the expected carbonation of the aged hydrated cement. Figure 3b targets the region $15 \leq 2\Theta$ [degree] ≤ 20, where the reflection at $2\Theta \approx 18.1$ degree corresponds to portlandite. This phase is present in almost all investigated fragments, in spite of the pozzolanic additives used in the cement formulation. The feature at $2\Theta \approx 9.2$ degree supports also the presence of a minor fraction of ettringite (PDF 41-1451) in some of the investigated fragments (see Figure 3c). Because of the less crystalline character of C-S-H, the assignment of this solid phases is not straight forward. For pure C-S-H phases, broad and less intense features are observed at $2\Theta \approx 29$ degree, which in this case overlap with one of the main features of calcite (see Figure 3a).
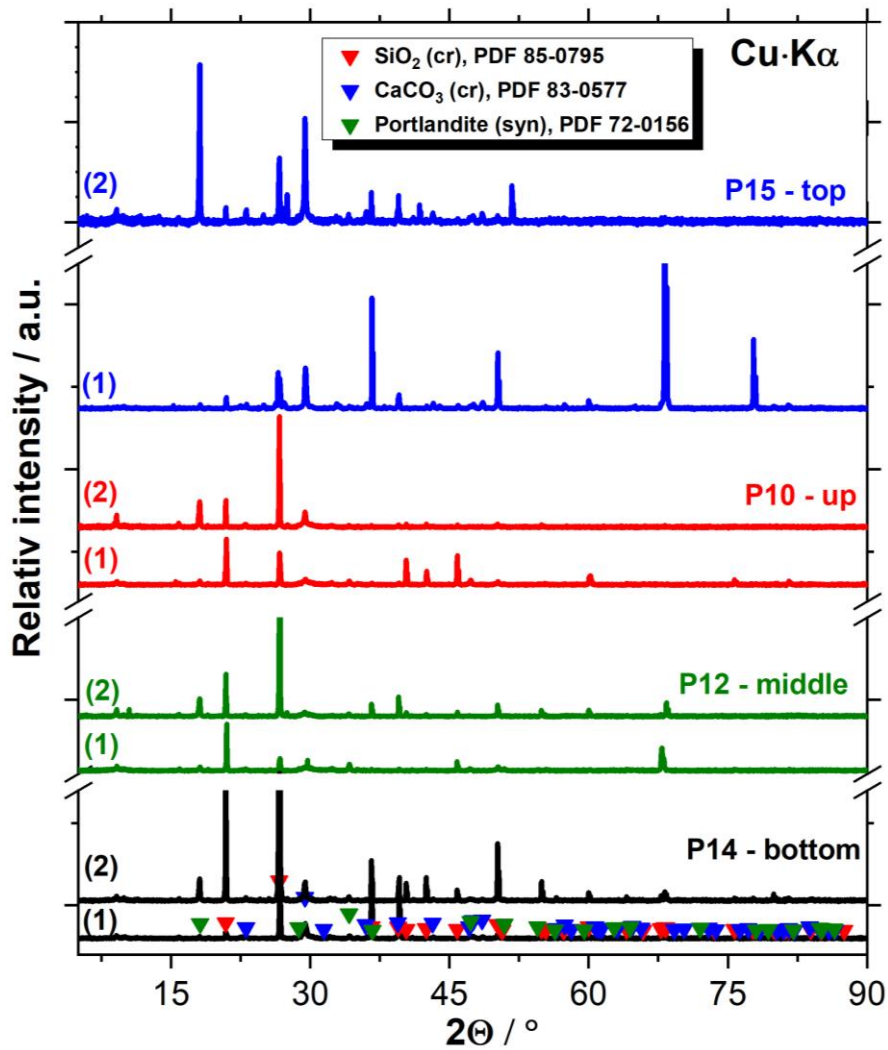
Figure 2. *Overview of the XRD patterns of all investigated cement fragments. Numbers (1) and (2) correspond to the two replicates investigated for each region. Red, blue and green symbols represent the peak positions of the quartz (PDF 85 – 0795), calcite (PDF 83 – 0577) and portlandite (PDF 72 – 0156), respectively.*
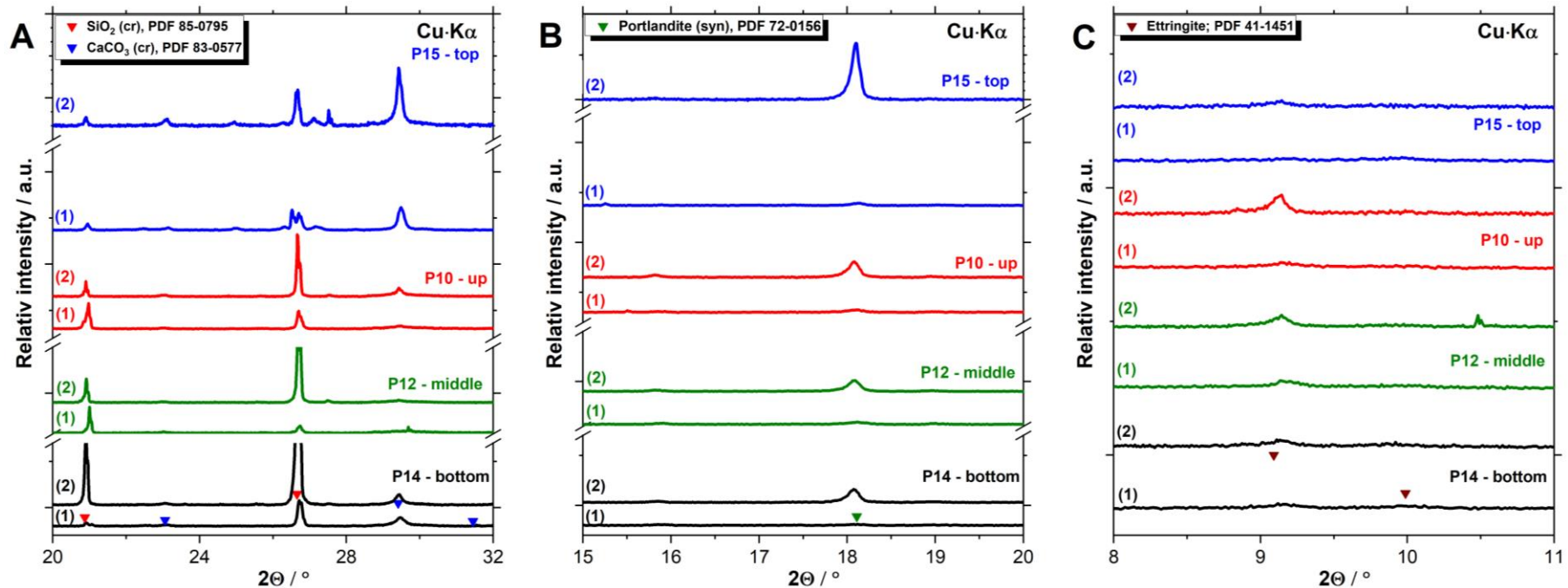
Figure 3. *Zoomed diffractograms of all investigated cement blocks for (a) $20 \leq 2\Theta$ [degree] ≤ 32, targeting main features of $SiO_2(cr)$ and calcite; (b) $15 \leq 2\Theta$ [degree] ≤ 20, targeting main features of portlandite; (c) $8 \leq 2\Theta$ [degree] ≤ 11, targeting main features of ettringite. Numbers (1) and (2) correspond to the two replicates investigated for each sub-sample. Symbols represent the peak positions of quartz (PDF 85 – 0795), portlandite (PDF 72 – 0156), calcite (PDF 83 – 0577) and ettringite (PDF 41 – 1451).*

The average crystallite size of the main phases identified in the investigated material was approximated using the Scherrer equation. The values quantified for quartz, calcite, portlandite and ettringite are summarized in Table 2. No clear trends can be identified for the different fragments investigated (top lid, up, middle, bottom) in terms of crystallite size. Except for the top fraction, quartz is generally the phase with significantly larger crystallite size, as expected considering that a large fraction of quartz sand was used in the formulation of the investigated cement (see Table 1).

Table 2: Crystallite size of phase components identified by XRD in the cement samples investigated in this work. The two values provided for each fraction correspond to the measurement of independent replicates. All values expressed in nm.

	Top lid (p15)	Up (p10)	Middle (p12)	Bottom (p14)
SiO_2	47 / 68	93 / 254	> 500	77 / > 500
$CaCO_3$	50 / 76	28 / 60	> 500 / 16	26 / 41
Portlandite	53 / 86	31 / 50	33 / 55	41 / 58
Ettringite	41 / 37	30 / 56	31 / 67	33 / 67

3.2 XPS

Figure 4 shows the XPS spectra powder samples made from parts of the four investigated cement fragments. Surface elemental composition (in atomic percent, at. %) determined from the spectra is reported in Table 3. The atomic distribution of the elements in the cement fragments do not show very significant deviations along the cement drum. As already indicated by XRD, XPS supports the ubiquitous presence of calcite in all investigated cement fragments. Note however that since XPS measurements were conducted under ambient conditions, the in-situ formation of calcite can also take place triggered by the presence of $CO_2(g)$ and humidity of the atmosphere. The spectra in Figure 4 and the quantitative values in Table 3 clearly show an increase in the Ca/Si ratio from top to the bottom of the investigated cement drum. Note however that these values do not reflect the true Ca/Si ratio in the C-S-H phases but rather an average ratio of the material, considering the inhomogeneity of the solid samples and in particular the presence of a large fraction of quartz sand.
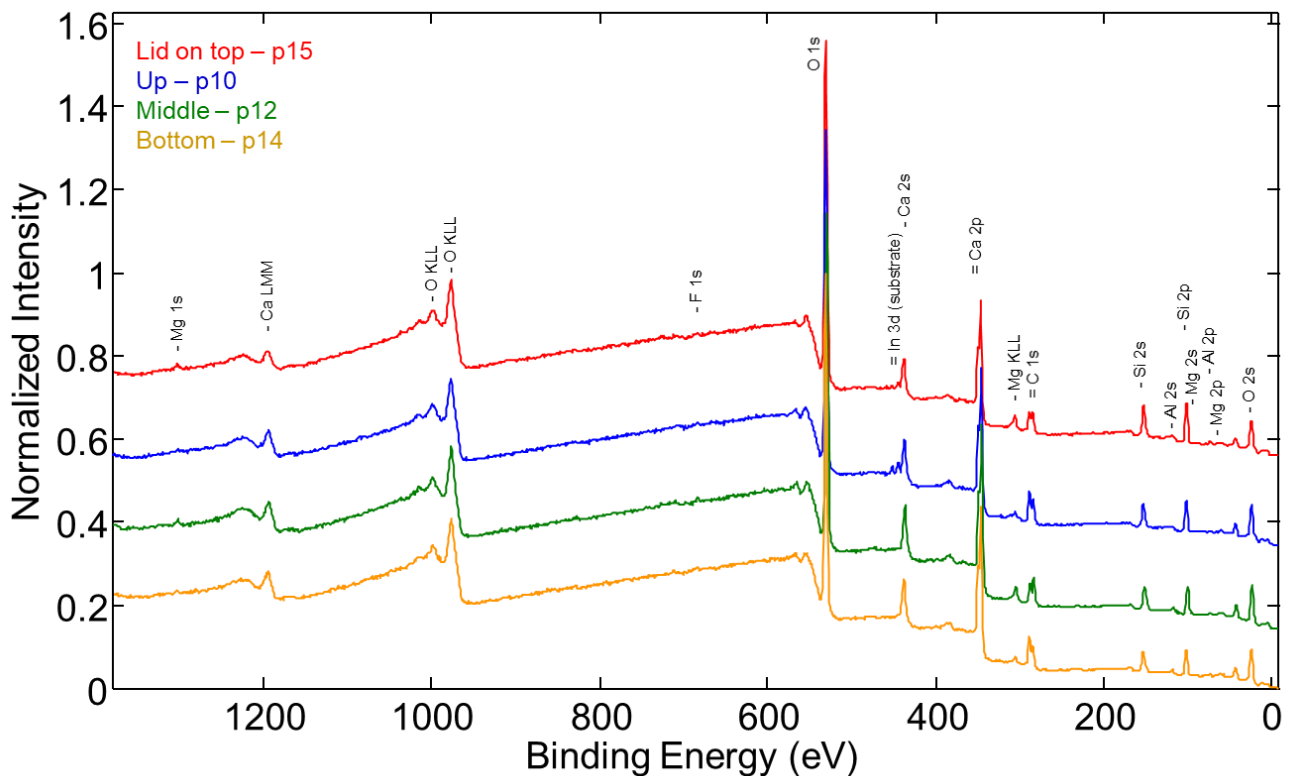

Figure 4. *XPS survey scan of the investigated cement fragments. Red, blue, green and yellow spectrum illustrate cement fragments from top lid (p15), upper (p10), middle (p12) and bottom (p14) of the waste drum.*

Table 3. Relative atomic concentration of the cement fragments. Relative error of (10±20) %.

Sample	C_{total}	C_{CO3}	O	F	Mg	Al	Si	S	Cl	Ca	Ca/Si
Top lid (p15)	15.0	7.2	62.0	0.2	0.5	0.8	11.6	0.3	0.1	9.5	0.81
Up (p10)	20.3	11.4	58.6	0.2	0.1	0.5	8.9	0.4	0.1	10.9	1.22
Middle (p12)	17.4	7.3	58.9	0.4	0.4	0.8	8.7	0.3	0.1	13.0	1.49
Bottom (p14)	20.0	10.9	59.5	0.1	0.2	0.5	7.6	0.2	0.1	11.7	1.54

Figure 5 displays the XPS spectra of C1 elemental lines of the four drum fragments. Main carbon peaks around 285, 287 and 289 keV are corresponding to organic carbon atoms (C_xH_y, C-O and C=O), and carbonate signals, respectively, which are in a good agreement with previous reports [3, 4]. The identification of organic carbon atoms is possibly related to organic additives in the cement formulation and adventitious hydrocarbon on the surface from the atmosphere. Further high-resolution spectrum from Al, Ca, Si and O are represented in the Appendix (see Figure A-1).
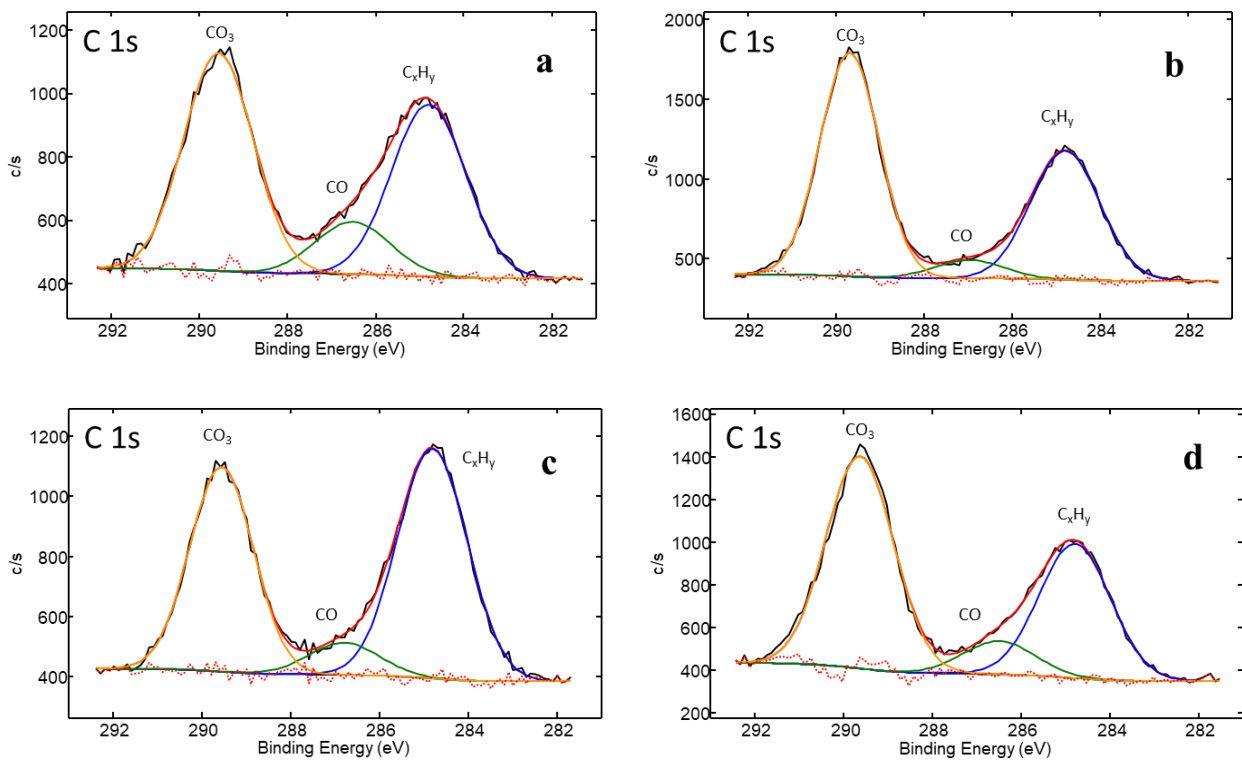

Figure 5. C 1s elemental lines collected for cement fragments from (a) lid top, (b) upper, (c) middle and (d) bottom regions of the waste drum. Unit of y-axis is intensity (counts per second: c/s).

3.3 TGA–DSC

Figure 6 shows the TGA and DSC analyses of the four cement fragments (two independent replicates each) investigated in this work. All fragments (top lid, up, middle, bottom of the cement drum) show a weight loss of ≈ 10 wt.% in the temperature range T = 30-250°C, corresponding to the cement free water loss and the loss of bound water in ettringite and C-S-H, as indicated in Figure 6 and Figure A-2 in the Appendix [7]. The water content is comparable between the two measurements for the upper cement sample, while slight differences in the water content are observed between both replicates in lid top and middle cement samples, thus supporting the heterogeneity of the material. As already hinted by XRD, TGA analyses confirm the presence of portlandite in all fragments, with the weight loss related to this phase occurring at ≈ 450°C as described in the literature [6, 7]. Lid top, middle and bottom cement fragments are characterized by a greater content of portlandite (weight loss of ≈ 2 wt.%), whereas a weight loss of ≈ 1 wt.% is determined for upper cement sample. The weight loss observed at T = 600-800°C is associated to the decarbonation of carbonate-containing cement phases (*e.g.*, calcite, monocarboaluminate, see Sections 3.1 and 3.2). This weight loss is well detected for the lid top (Δwt. ≈ 4 wt.%) and bottom (Δwt. ≈ 2.4 wt.%) cement samples, while the weight loss is ≤ 0.5% for the upper and middle cement samples. The presence of quartz, detected in the XRD analysis (see section 3.1) is also confirmed by TGA-DSC. DSC shows for all fragments an endothermic process occurring at T ≈ 600 °C, which is presumably associated to the transitions "quartz β→α" as also reported in [2].
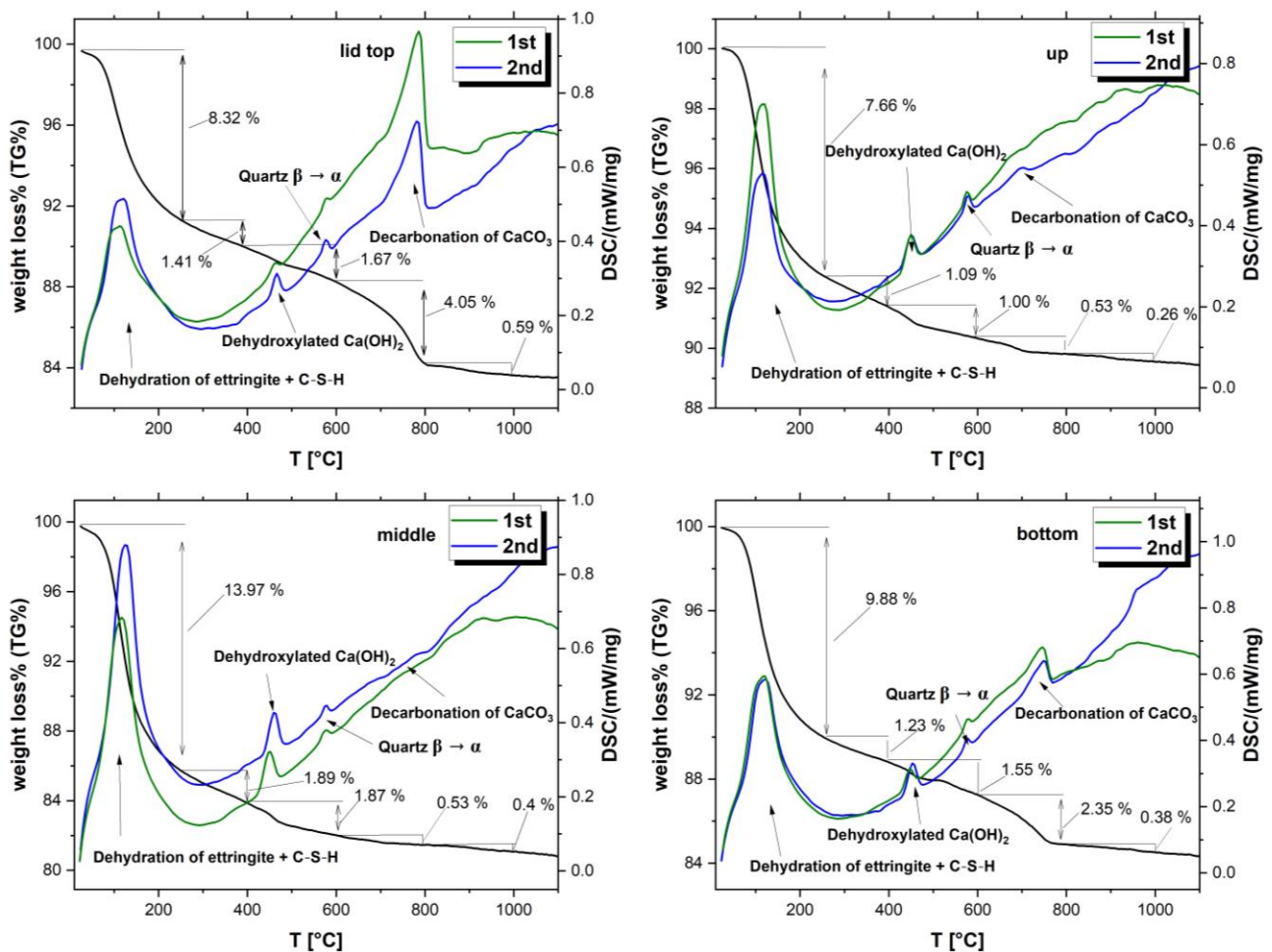
Figure 6. *TGA-DSC curves determined for the four cement fragments investigated. Green and blue lines correspond to the first and second DSC replicates of each sample. Weight loss data (second replicate) represented in black line. Data collected with a heating rate of 10 K/min.*

3.4 µ–CT, SEM–EDS and pore characterization

Figure 7 shows SEM pictures collected for all investigated samples. All pictures reflect the heterogeneity of the cementitious material. Large quartz particles, as well as the holes left by the detachment of these particles, are observed in all cement fragments. Rods and fibers also observed, which are tentatively assigned to calcite and ettringite. Figure 8 shows EDS data collected for a region in the upper fragment of the cement drum (sample p10). In combination with the quantitative evaluation (see figure caption), this characterization confirms the predominance of C-S-H phases with the inclusion of well-defined Si-rich particles, which underpin the predominance of unreacted quartz. The average composition of this fragment points also to the presence of carbon atoms (expectedly in the form of calcite or AFm phases), as well as a lower content (< 1 at.%) in Al, S and Fe. The latter observation points to the presence of a minor fraction of ettringite and AFt phases. The presence of the latter phases is clearly evidenced in Figure 9, which shows the EDS data collected for the top lid sample (p15).
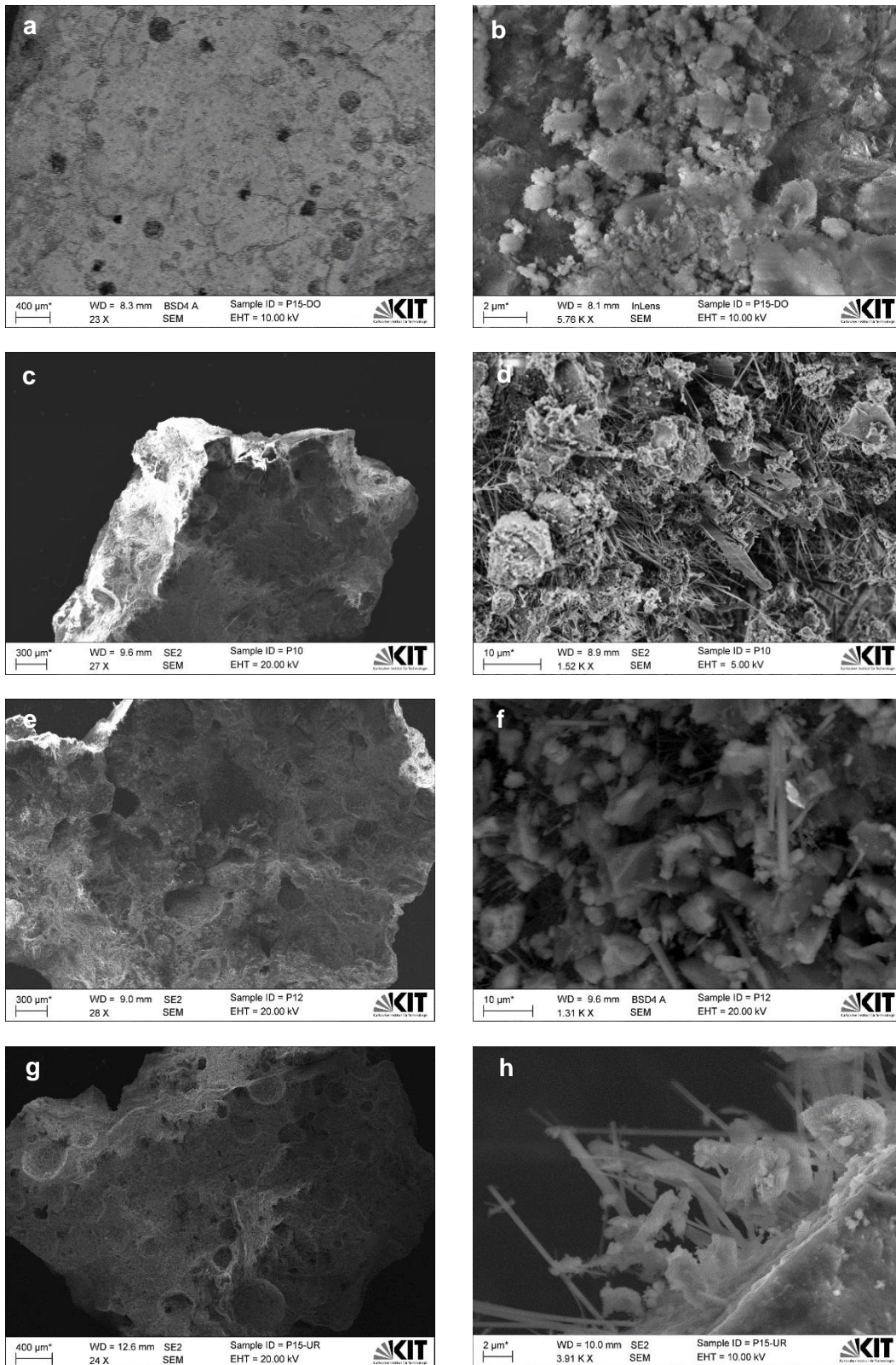
Figure 7. SEM secondary electron images collected for all cement fragments investigated in this work: (a), (b) lid on top; (c), (d) upper region; (e), (f) middle region; (g), (h) bottom region
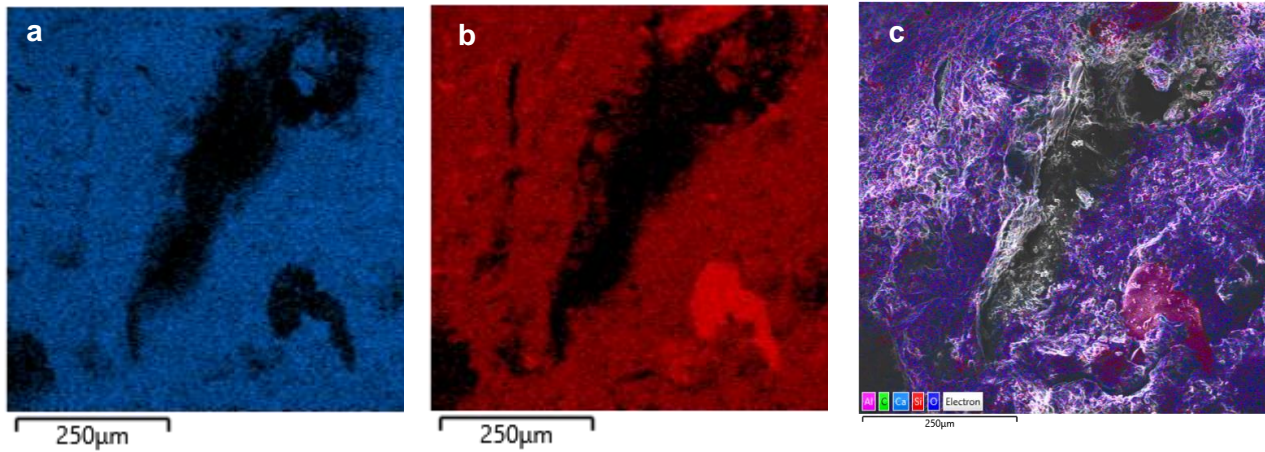
Figure 8. *EDS mapping collected for the upper fragment of the cement drum (sample p10), showing: (a) the Ca Kα1 line, (b) the Si Kα1 line and (c) an EDS layered image. Average composition of the sample quantified as (in atomic %): O: 62%, Ca: 14%, C: 13%, Si: 9.7%, Al: 0.9%, S: 0.4%, Fe: 0.3%. Elemental composition in the Si-rich particle: O: 69%, Ca: 1%, Si: 30%.*
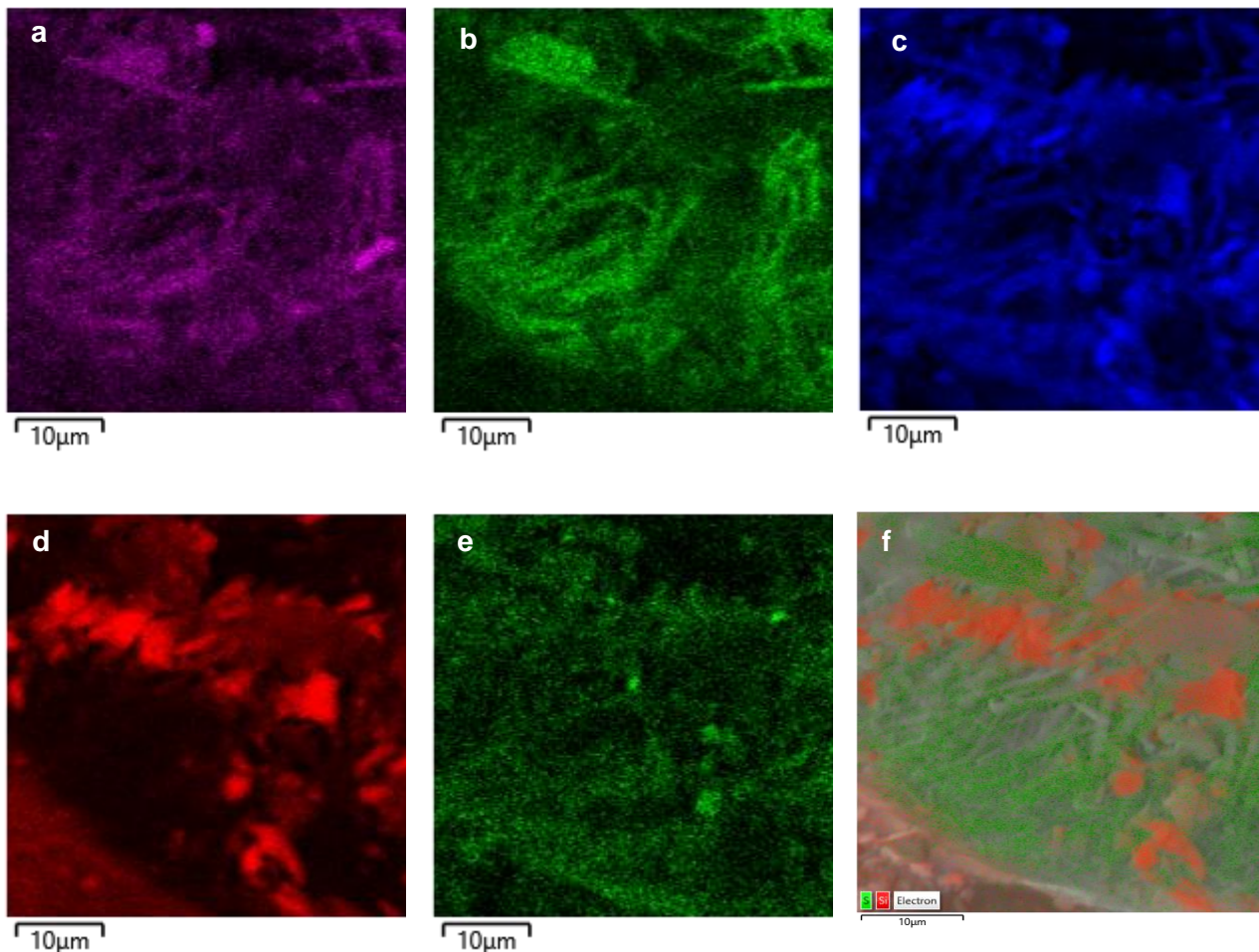

Figure 9. *EDS mapping collected for the lid top of the cement drum (sample p15), showing: (a) the Al Kα1 line, (b) S Kα1 line, (c) O Kα1 line, (d) Si Kα1 line, (e) C Kα1,2 line and (f) an EDS layered image. Average composition of the sample quantified as (in atomic %): O: 69%, Ca: 15%, C: 10%, Si: 1.9%, Al: 1.6%, S: 1.9%.*

Figure 10 shows the µ-CT imaging collected for the upper fragment of the cement drum (sample p10). The pictures show two well-defined regions, characterized by two different porosities. Similar observations are obtained for the lid top cement fragment (sample p15), but two separate regions could not be identified in the µ-CT imaging collected for the middle cement fragment (sample p12). The altered regions appear to have less porosity. In general, porosity is between 1% and 8% in volume, with a number of pores between 2 and 10 pores·mm^{-3} and average size of 10–20 µm. Information on the size distribution of the pores is provided in Figure 11.
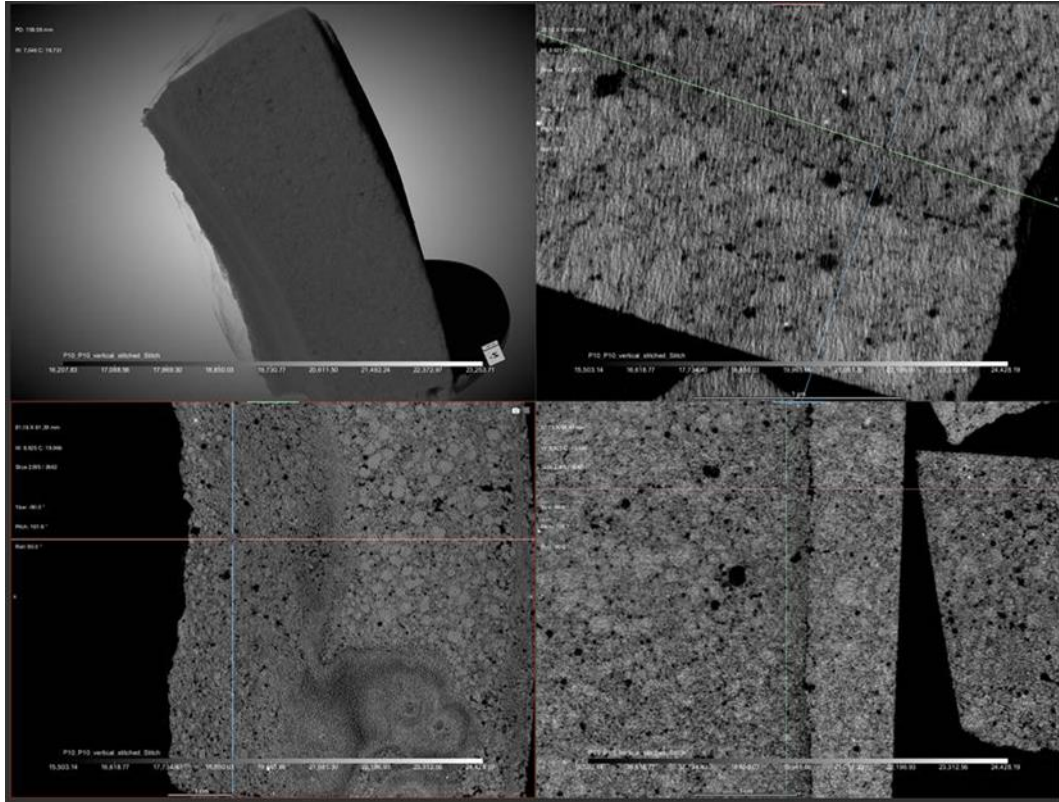

Figure 10. *Microtomography collected for the upper fragment (sample p10) of the investigated cement drum provided by PSI.*
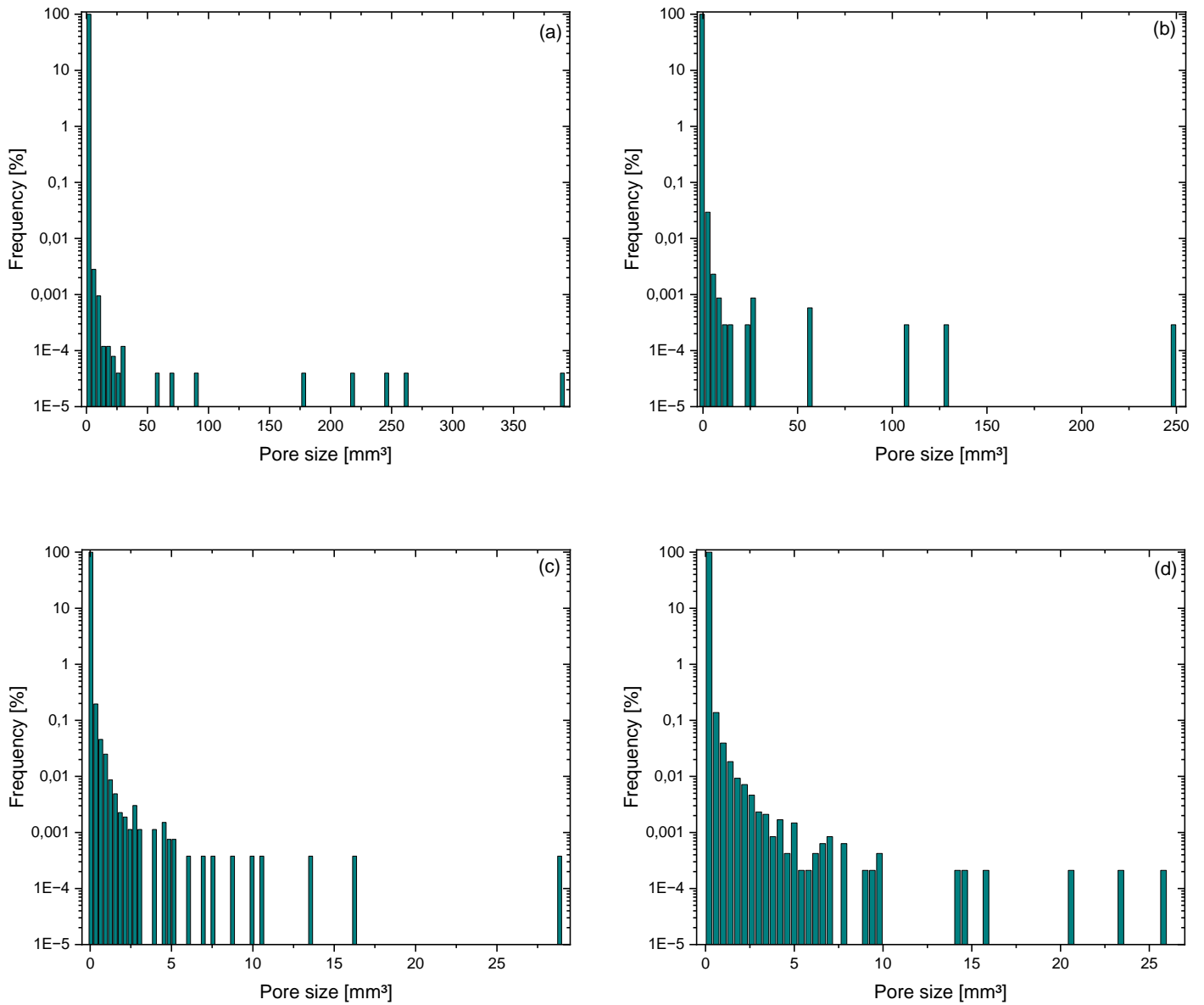
Figure 11. *Pore size distribution determined for the cement drum (a) upper fragment; (b) middle fragment (c) and (d) top lid.*

4 Summary and conclusions

A LLW cemented waste drum stored since 1994 at the Swiss Federal Interim Storage Facility (BZL), operated by PSI, was mainly characterized by KIT-INE. This report summarizes the characterization results obtained at KIT-INE. After the selection of one of the drums by the project partners and the approval of the Swiss Federal Nuclear Safety Inspectorate (ENSI), cement samples from four different locations in the drum (bottom, middle, upper, top lid) were collected by PSI and sent to KIT-INE. A thorough characterization of the different drum fragments was conducted with a diversity of methods available at KIT-INE, including X-ray diffraction (XRD), thermogravimetric analysis coupled to differential scanning calorimetry (TG-DSC), X-ray photoelectron spectroscopy (XPS), scanning electron microscopy and energy dispersive X-ray spectroscopy (SEM-EDS), as well as micro computed tomography (μ-CT). Characterization methods consistently confirm the heterogeneity of the samples, although four main crystalline phases are identified, *i.e.*, quartz, portlandite, calcite and ettringite. In spite of their predominantly amorphous character, C-S-H phases are evidenced by XRD, TGA-DSC as well as by the elemental analysis by SEM-EDS. A large fraction of unreacted quartz is identified in the form of large crystalline particles, with crystallite size in the range of 50 to > 500 nm. No clear trends are observed along the investigated drum, with the exception of a systematic decrease in the overall Ca:Si ratio from the top to the bottom of the cemented drum. Insights on the porosity of the material are obtained by μ-CT, with the identification of two main regions of manifestly different porosity.

Acknowledgments

REFERENCES

[1]   Ahlrichs, R., Furche, F., and Grimme, S., 2000. Comment on "Assessment of exchange correlation functionals"[AJ Cohen, NC Handy, Chem. Phys. Lett. 316, 160–166]. Chemical Physics Letters, 325, (1-3): p. 317-321.

[2]   Chu, H., Wang, Z., Zhang, Y., Wang, F., Ju, S., Wang, L., and Wang, D., 2020. Using Graphene Sulfonate Nanosheets to Improve the Properties of Siliceous Sacrificial Materials: An Experimental and Molecular Dynamics Study. Materials, 13, (21): p. 4824.

[3]   Dammaschke, T., Gerth, H.U., Züchner, H., and Schäfer, E., 2005. Chemical and physical surface and bulk material characterization of white ProRoot MTA and two Portland cements. Dental Materials, 21, (8): p. 731-738.

[4]   Haselbach, L.M.and Ma, S., 2008. Potential for carbon adsorption on concrete: Surface XPS analyses. Environmental science & technology, 42, (14): p. 5329-5334.

[5]   Holzwarth, U.and Gibson, N., 2011. The Scherrer equation versus the'Debye-Scherrer equation'. Nature nanotechnology, 6, (9): p. 534-534.

[6]   L'hôpital, E., Lothenbach, B., Le Saout, G., Kulik, D., and Scrivener, K., 2015. Incorporation of aluminium in calcium-silicate-hydrates. Cement and Concrete Research, 75: p. 91-103.

[7]   Lothenbach, B., Durdzinski, P., and De Weerdt, K., 2016. Thermogravimetric analysis. A practical guide to microstructural analysis of cementitious materials, 1: p. 177-211.

[8]   Moulder, J., Stickle, W., Sobol, P., and Bomben, K., 1995.Handbook of X-ray Photoelectron Spectroscopy, (Eds.: Chastain, J.; King Jr., R.C.) ULVAC-PHI Inc, Japan; Physical Electronics (USA). Inc.

[9]   Naumkin, A.V., Kraut-Vass, A., Garenstroom, S.W., and Powell, C.J., 2000. NIST X-ray Photoelectron Spectroscopy Database, NIST Standard Reference Database Number 20, National Institute of Standards and Technology, Gaithersburg MD, 20899.

[10]   Pantoja-Cortes, J., Sanchez-Bajo, F., and Ortiz, A.L., 2012. A line-broadening analysis model for the microstructural characterization of nanocrystalline materials from asymmetric x-ray diffraction peaks. Journal of Physics: Condensed Matter, 24, (21): p. 215301.

[11]   Scherrer, P., 1918. Göttinger nachrichten math. Phys, 2: p. 98-100.

[12]   Seah, M., Gilmore, I., and Beamson, G., 1998. XPS: binding energy calibration of electron spectrometers 5—re-evaluation of the reference energies. Surface and Interface Analysis: An International Journal devoted to the development and application of techniques for the analysis of surfaces, interfaces and thin films, 26, (9): p. 642-649.
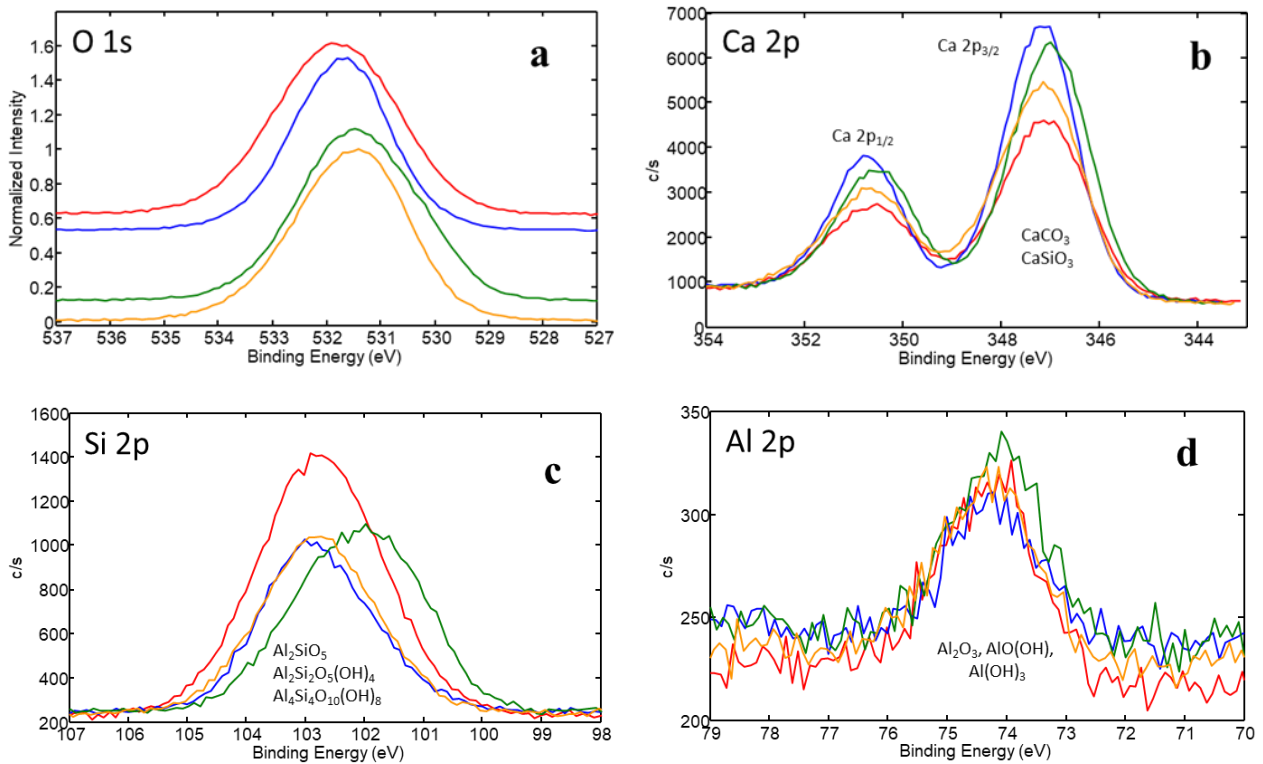
Appendix

Figure A-1: *High-resolution spectrum of (a) O 1s, (b) Ca 2p, (c) Si 2p and (d) Al 2p of cement blocks. Red, blue, green and yellow spectrum illustrate cement fragments from lid top (p15), upper (p10), middle (p12) and bottom (p14) of the waste drum. Compounds with similar binding energies of elemental lines are indicated.*
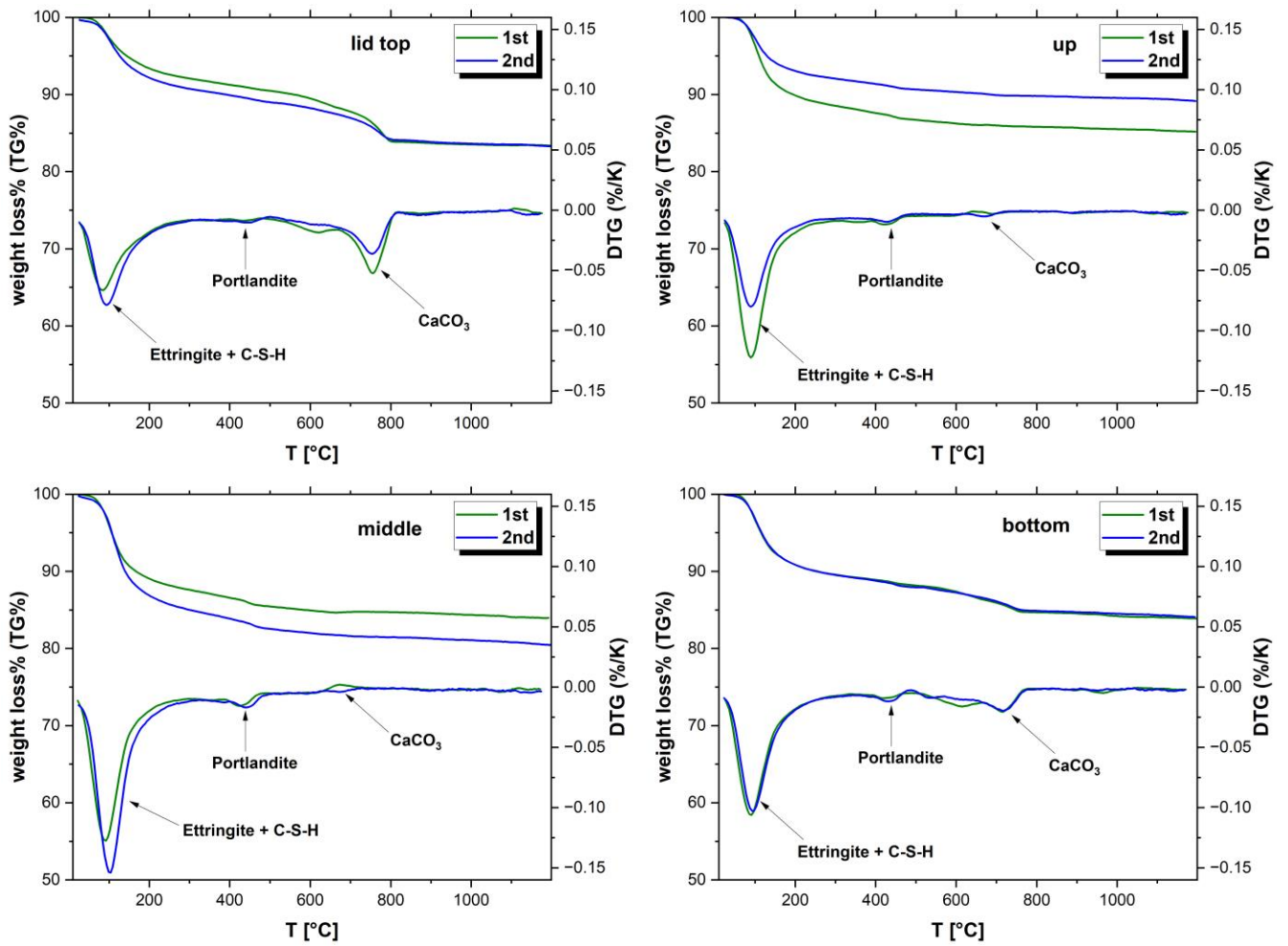
Figure A-2: *TGA-DTG curves determined for the four cement fragments investigated. Green and blue lines correspond to the first and second replicates of each sample. Data collected with a heating rate of 10 K/min.*